

Dislocation structure and crystallite size-distribution in hexagonal nanomaterials from X-ray peak profile analysis

Tamás Ungár¹ and Jenő Gubicza^{1,2}

¹Department of General Physics, Eötvös University Budapest, P.O.B. 32, H-1518, Hungary

²Department of Solid State Physics, Eötvös University Budapest, P.O.B. 32, H-1518, Hungary

The microstructure of three different nanocrystalline materials with hexagonal crystal structure are studied by X-ray diffraction peak profile analysis. The crystallite size distribution and the dislocation structure are determined in plasmathermal silicon nitride powder, sintered tungsten carbide and severely deformed titanium and are compared with transmission electron microscopy (TEM) results. In the case of the silicon nitride powder the particle size determined by TEM is in good correlation with the coherently scattering domain size provided by X-rays. In the case of bulk titanium the crystallite size given by X-rays correlates well with the dislocation cell size obtained by TEM. It is found that in tungsten carbide the dominant dislocation slip system is basal, whereas, in plastically deformed titanium the basal slip is practically absent with the dominance of pyramidal dislocations in good correlation with other investigations of the literature.

Keywords: crystallite size distribution, dislocation structure, X-ray peak profile analysis, hexagonal crystals, nanostructure.

Short title: T. Ungár & J. Gubicza: Dislocations and crystallite size in hexagonal materials

1 Introduction

The relationship between the microstructure and the physical properties of nanostructured materials is in due focus of materials science. The first step to understand the correlation between the microstructure and the mechanical, magnetic and thermal properties of nanomaterials is the correct characterization of their microstructure. This can be done on the submicron to a few microns scale of specimen size by transmission electron microscopy (TEM) or on the millimeter scale of specimen size by X-ray diffraction (XRD) peak profile analysis. The two different techniques sample very different specimen volumes, thus providing different details and different averages of the parameters characterising the microstructure. On the other hand, for the correct interpretation of the results obtained by either of the two methods the application of the counterpart can be very helpful and in some cases even mandatory.

A large number of recent papers have shown that the crystallite size and size-distribution and the dislocation structure can be well characterised by X-ray diffraction peak profile analysis [1-11]. X-ray diffraction peak profiles are broadened due to small crystallite size and lattice distortions. The two effects can be separated on the basis of the different diffraction order dependence of peak broadening. The standard methods of

peak profile analysis based on the full widths at half maximum (FWHM), the integral breadths and the Fourier coefficients of the profiles provide the apparent crystallite size and the mean square strain [12-14]. Peak broadening is further complicated by strain anisotropy. This means that neither the FWHM nor the integral breadth nor the Fourier coefficients of the profiles are monotonous functions of the diffraction vector [15-16]. It has been shown recently that strain anisotropy can be well accounted for by the dislocation model of the mean square strain by introducing the contrast factors of dislocations [1,2,4-6,17-19]. Since the values of the dislocation contrast factors depend on the dislocation slip systems present in the crystal, under certain circumstances, the evaluation of X-ray profiles for the contrast factors enables the determination of the dislocation structure. An evaluation procedure of X-ray diffraction profiles was elaborated recently for the determination of crystallite size distribution and the dislocation structure in nanostructured materials [10-11]. In this method, the Fourier coefficients of the measured physical profiles are fitted by the Fourier coefficients of physically based theoretical functions of size and strain profiles.

In this paper the microstructure of three nanocrystalline specimens with hexagonal crystal structure are studied by X-ray peak profile analysis. The mean crystallite size, the size distribution and the dislocation structure of silicon nitride ceramic powders, sintered tungsten-carbide and plastically deformed titanium are determined and compared with the results obtained by other methods, especially by TEM.

2. Experimentals

2.1. Sample preparation

Nanodisperse silicon nitride powder was synthesized by the vapor-phase reaction of silicon tetrachloride and ammonia in a radiofrequency thermal plasma reactor under conditions given previously [20]. The as-synthesized powder was subjected to a two-step thermal processing to remove NH₄Cl and Si(NH)₂ by-products formed due to the NH₃ excess in the plasma synthesis. The powder was treated in nitrogen at 400°C for 1 h and subsequently at 1100°C for 1 h to achieve the complete decomposition of by-products. The powder was predominantly amorphous with a crystalline content of about 20vol%. The crystallization was performed in a horizontal laboratory furnace in flowing nitrogen at 0.1 MPa, at annealing temperatures of 1250, 1350, 1450 and 1500°C for 2 h.

A nanocrystalline tungsten-carbide specimen was manufactured by the following processing steps. Tungsten-carbide powder with submicron grain-size was mixed with wax and acetone and subjected to high energy ball-milling producing nanocrystalline powder. The milled powder was compacted under a pressure of 190 MPa to a density of about 50%. Sintering was carried out on the compacted sample at 1420°C and 7 MPa. The sintered specimen had a relative density of 92%.

A nanostructured titanium specimen was produced by severe plastic deformation (SPD). The deformation was carried out by pressing a Ti billet with an average grain size of 10 µm through a 90° ECAP die following route B_C for 8 passes at 400-450°C [21]. The ECAP was followed by cold rolling at room temperature to 73% reduction in cross-section area.

2.2. X-ray diffraction technique

The diffraction profiles were measured by a special double crystal diffractometer with negligible instrumental broadening [22]. A fine focus rotating cobalt anode, Nonius FR 591, was operated as a line focus at 36 kV and 50 mA. The symmetrical 220 reflection of a Ge monochromator was used in order to have wavelength compensation at the position of the detector. The $K\alpha_2$ component of the Co radiation was eliminated by an 0.16 mm slit between the source and the Ge crystal. The profiles were registered by a linear position sensitive gas flow detector, OED 50 Braun, Munich. For titanium the X-ray diffractograms were measured by a Philips X'pert powder diffractometer using Cu anode and pyrolitic graphite secondary monochromator. The instrumental corrections were carried out by the Stokes method [23] using Si standard (NBS 640).

3. Evaluation procedure of the X-ray peak profiles

According to the kinematical theory of X-ray diffraction, the physical profile of a Bragg reflection is given by the convolution of the size and the distortion profiles [13]

$$I^P = I^S * I^D, \quad (1)$$

where the superscripts S and D stand for size and distortion, respectively. The Fourier transform of this equation gives [13]

$$A(L) = A^S(L) A^D(L), \quad (2)$$

where $A(L)$ are the absolute values of the Fourier coefficients of the physical profiles, A^S and A^D are the size and the distortion Fourier coefficients and L is the Fourier variable. Assuming that in the crystal the lattice distortions are caused by dislocations A^D can be given in the form [17-19]

$$A^D(L) = \exp[-\rho BL^2 f(\eta) g^2 \bar{C}], \quad (3)$$

where L is the Fourier variable, $B=\pi b^2/2$, b is the absolute value of the Burgers vector, ρ is the dislocation density, $\eta \sim L/R_e$, R_e is the effective outer cut-off radius of dislocations, g is the absolute value of the diffraction vector, \bar{C} is the average dislocation contrast factor and $f(\eta)$ is a function derived explicitly by Wilkens [19]. Instead of R_e , it is physically more appropriate to use the parameter $M = R_e \sqrt{\rho}$ defined by Wilkens as the dislocation arrangement parameter [19]. The value of M gives the strength of the dipole character of dislocations: the higher the value of M , the weaker the dipole character and the screening of the displacement fields of dislocations. It can be shown that for a hexagonal polycrystalline specimen \bar{C} can be given in the following form [24]:

$$\bar{C} = \bar{C}_{hk0} [1 + q_1 x + q_2 x^2], \quad (4)$$

where $x = (2l^2)/(3a^2 g^2)$, a is the lattice parameter in the hexagonal basal plane, l is the fourth index of reflection, q_1 and q_2 are parameters depending on the elastic constants and on the dislocation slip systems active in the crystal [24].

It was observed by many authors that in powder or bulk nanostructured materials, the crystallite-size distribution can be described by log-normal function [25-29]. Assuming spherical crystallite shape with log-normal size distribution, the Fourier transform of the size profile can be given as [10,11]:

$$A^S(L) \sim \frac{m^3 \exp(4.5\sigma^2)}{3} \operatorname{erfc}\left[\frac{\ln(|L|/m)}{\sqrt{2}\sigma} - 1.5\sqrt{2}\sigma\right] - \frac{m^2 \exp(2\sigma^2)|L|}{2} \operatorname{erfc}\left[\frac{\ln(|L|/m)}{\sqrt{2}\sigma} - \sqrt{2}\sigma\right] + \frac{|L|^3}{6} \operatorname{erfc}\left[\frac{\ln(|L|/m)}{\sqrt{2}\sigma}\right], \quad (5)$$

where σ is the variance and m is the median of the log-normal size distribution function and erfc is the complementary error function. The arithmetic, the area- and the volume-weighted mean crystallite sizes are obtained from σ and m as [29]:

$$\langle x \rangle_{\text{arit}} = m \exp(0.5 \sigma^2), \quad (6)$$

$$\langle x \rangle_{\text{area}} = m \exp(2.5 \sigma^2), \quad (7)$$

$$\langle x \rangle_{\text{vol}} = m \exp(3.5 \sigma^2). \quad (8)$$

A numerical procedure has been worked out for fitting the Fourier transform of the experimental profiles by the product of the theoretical functions of size and strain Fourier transforms given in Eqs. (3) and (5) [10,11]. The method has the following steps: i) the Fourier coefficients of the experimental profiles have been calculated by a non-equidistant sampling Fourier transformation, ii) the instrumental correction was carried out by the Stokes method [23] using Si standard (NBS 640), iii) the Fourier coefficients of the size and strain profiles were calculated by using Eqs. (3)-(5), iv) the corrected experimental and the calculated Fourier coefficients were compared by the least squares method. The measured and the fitted Fourier coefficients for titanium sample investigated in this paper are shown in Fig. 1. The difference between the measured and the fitted values are also shown in the figure. The procedure has six fitting parameters for hexagonal crystals: (i) the median and the variance, m and σ , of the log-normal size distribution function, (ii) the density and the arrangement parameter of dislocations, ρ and M , and (iii) the q_1 and q_2 parameters in the contrast factors of dislocations.

4. Results and discussion

4.1. The effect of crystallization temperature on the grain size distribution of silicon nitride

The amorphous phase content of the silicon nitride powders is shown in Table 1. In the as-synthesized powder the amorphous phase content is 80vol%. As the temperature of crystallization increases, the amount of the amorphous phase decreases. After the crystallization at 1500°C the amorphous phase content is only 20vol%. The median, the

variance of the grain size distribution, the area-weighted mean grain size of the crystalline fraction, $\langle x \rangle_{\text{area}}^c$, of the powders determined from X-ray profile analysis are listed in Table 1.

Denoting the area-weighted mean grain-size of the entire powder by $\langle x \rangle_{\text{area}}^t$ (this is a total average over the crystalline and amorphous phases) the area-weighted mean grain-size of the amorphous phase, $\langle x \rangle_{\text{area}}^a$, can be calculated from $\langle x \rangle_{\text{area}}^t$ and $\langle x \rangle_{\text{area}}^c$ according to equations (6) and (7) in [28]. The values of $\langle x \rangle_{\text{area}}^t$ has been determined from the specific surface area of the powder, where latter was obtained by the BET (Brunauer-Emmett-Teller) method [30]. The $\langle x \rangle_{\text{area}}^t$ values are listed in Table 1. The determination of the area-weighted mean grain-size of the amorphous fraction for the samples having small amount of amorphous phase is uncertain, therefore it was determined only for the powders having high amorphous phase contents. The values of the amorphous mean grain-size are 31, 45 and 49 nm for the as-synthesized sample, the powders heat-treated at 1250 and 1350°C, respectively. It can be established that in these samples the average grain size of the amorphous phase is lower than that of the crystalline fraction and it increased during heat-treatments. The average size of the crystalline grains decreased slightly at temperatures up to 1450°C probably because of the crystallization of the smaller amorphous grains, while it significantly increased during heat-treatment at 1500°C (see Fig. 2). The average grain-size of the entire powder $\langle x \rangle_{\text{area}}^t$ increased with increasing temperature that is caused by the grain-coarsening in the amorphous phase and the increase of the amount of the crystalline phase having large grains. For the powder having high amount of crystalline phases (crystallized at 1500°C) the average grain-size of the crystalline fraction obtained by X-rays agrees well with that of the entire powder calculated from the specific surface area.

The log-normal size-distribution function corresponding to the m and σ values for the powder heat-treated at 1500°C is shown as a solid line in Fig. 3. The size distribution of the grains in the entire powder was examined by TEM [28]. The size distribution obtained from the TEM micrographs is shown as bar-graph in Fig. 3. (The scales of the bar-diagram and the size-distribution function are on the left- and the right hand side of the figure.) In the TEM measurements 300 particles were chosen at random in different areas in the powder. The agreement between the bar-diagram and the size-distribution function is relatively good. The small quantitative difference between the X-ray and the TEM results is probably due to the facts that the bar-diagram was obtained from a relatively small number of grains and that the smaller particles of the amorphous phase were not taken into account in the size distribution function determined by X-rays. About five orders of magnitude more grains contribute to the X-ray measurements. To increase the number of grains for counting in TEM micrographs would need considerably greater efforts.

4.2. Dislocation structure and crystallite size distribution of sintered tungsten-carbide

The dislocation density, ρ , was found to be $1.5 \pm 0.1 \cdot 10^{16} \text{ m}^{-2}$ in tungsten-carbide. The average distance between the dislocations equals to $8.2 \pm 0.8 \text{ nm}$. The median and the variance of the crystallite size distribution are $m=21 \pm 2 \text{ nm}$ and $\sigma=0.57$, respectively. The arithmetic mean crystallite-size calculated from m and σ is $25 \pm 3 \text{ nm}$ which means that the crystallites contain about three dislocations in average. The area-, and the

volume weighted mean crystallite sizes are 47 ± 5 and 65 ± 6 nm, respectively. The crystallite size distribution and the mean crystallite sizes are shown in Fig.4.

The values of q_1 and q_2 of the contrast factors for tungsten-carbide sample determined from the fitting procedure are $q_1=-0.75\pm0.02$ and $q_2=0.56\pm0.02$. The values of q_1 and q_2 for the possible slip systems in tungsten-carbide were calculated according to the formulas for elastically isotropic crystals given by Klimanek and Kuzel [1]. Elastic isotropy has been assumed, since, to the best knowledge of the authors, the anisotropic elastic constants of tungsten-carbide are not available. The isotropic q_1 and q_2 were evaluated with $E=707$ GPa and $v=0.18$ [26] and are listed in Ref.[31]. It has been found that the experimentally determined values of q_1 and q_2 are close to the values corresponding to basal slip. The q parameter values of the basal slip system populated by edge dislocations are: $q_1=-0.96$ and $q_2=0.83$. From this we concluded that the dominant dislocation type in the investigated tungsten-carbide specimen is basal edge: $\langle 11\bar{2}0 \rangle \{0001\}$.

4.3. Microstructure of severely deformed titanium

The microstructural parameters of deformed titanium obtained from the fitting of the Fourier coefficients of the X-ray diffraction profiles, cf. [12,32,34], are: $m=38\pm3$ nm, $\sigma=0.49\pm0.05$, $\rho=0.86\pm0.08 \cdot 10^{15} \text{ m}^{-2}$, $q_1=-0.05\pm0.02$ and $q_2=0.18\pm0.02$. The arithmetic, the area- and the volume-weighted mean crystallite sizes calculated from the values of m and σ by using Eqs. (6)-(8) are 43 ± 4 , 69 ± 7 and 88 ± 9 nm, respectively. It can be established that the severe plastic deformation of titanium resulted in nanocrystalline (or submicron grain size) material. The microstructure of the ECA pressed Ti specimen was also investigated by TEM [32]. A good correlation is found between the arithmetic mean crystallite size determined from X-ray diffraction, 43 nm, and the mean dislocation cell size, 45 nm obtained from TEM micrographs [32]. The average dislocation density obtained from TEM is $1.02 \cdot 10^{15} \text{ m}^{-2}$. Although the dislocation density measured from TEM is from small local areas, it agrees well with that calculated from X-ray analysis.

The q_1 and q_2 parameters of the contrast factors depend on the character of dislocations, and therefore enable the determination of the prevailing dislocation slip systems in the sample. The q_1 and q_2 values for the 11 most probable slip systems in Ti according to Jones and Hutchinson [33] and Kuzel and Klimanek [1] are listed in Ref.[34]. The experimental q_1 and q_2 values for titanium do not match any single pair of the q_1 and q_2 parameters calculated theoretically. This indicates that more than one dislocation slip system are activated during deformation. Due to the linear superposition of the displacement fields of different dislocations, the effective contrast factors, \bar{C} , can be calculated as the weighted average of the contrast factors of the individual slip systems, \bar{C}_i :

$$\bar{C} = \sum_i f_i \bar{C}_i , \quad (9)$$

where f_i is the population fraction of dislocation system i. The f_i values should satisfy the following equation:

$$\sum_i f_i = 1. \quad (10)$$

Substituting the formula for hexagonal contrast factors in Eq. (4) into Eq. (9), we obtain two equations for q_1 and q_2 [24]:

$$q_1 = (\sum_i q_{1,i} \cdot f_i \cdot \bar{C}_{hk0,i}) / (\sum_i f_i \cdot \bar{C}_{hk0,i}) \quad (11)$$

$$q_2 = (\sum_i q_{2,i} \cdot f_i \cdot \bar{C}_{hk0,i}) / (\sum_i f_i \cdot \bar{C}_{hk0,i}) \quad (12)$$

The population fractions of the dislocation systems can be calculated by substituting the measured q_1 and q_2 values in the left-hand sides of Eqs. (11) and (12). Since there are only three independent equations, Eqs. (10)-(12) can be solved at a time only for the f_i values of three slip systems. In order to solve this problem, a trial-and-error method was worked out [24].

According to previous investigations, two types of dislocations exist in deformed titanium: “type $\langle\bar{a}\rangle$ ”, where the Burgers vector of dislocations is parallel to the hexagonal “a” axis and “type $\langle\bar{c}+\bar{a}\rangle$ ”, where the Burgers vector has components in both the hexagonal “a” and “c” directions. It has been shown by TEM that the possible $\langle\bar{c}+\bar{a}\rangle$ type slip systems are Py4E and/or Py2S [33]. In hexagonal crystals, the possible $\langle\bar{a}\rangle$ type slip systems are: PyE, PrE, BE and BS [1,24,33] (E and S refer to edge and screw dislocations, and Py, Pr and B to pyramidal, prismatic and basal, respectively). For each calculation, a set of three slip systems (trios) were selected from these six slip systems, resulting in a total of 20 possible permutations. Eqs. (10)-(12) were solved for the f_i values for each of the trios. In 13 cases out of the 20 permutations, at least one of the f_i values were negative, which is physically unrealistic. Therefore, these cases were discarded. For the seven physically realistic solutions, in which all the f_i values were non-negative, the fraction of the Py4E slip system, which is $\langle\bar{c}+\bar{a}\rangle$ type, is about 2/3 and the rest of dislocations are $\langle\bar{a}\rangle$ type [34]. Jones and Hutchinson claim the presence of screw dislocations in Ti [29]. The only configuration from the seven solutions that contains considerable amount of screw dislocations is 67±5% Py4E + 22±5% PrE + 11±5% BS [34]. The dominance of the “pyramidal edge 4 (Py4E)” in the $\langle\bar{c}+\bar{a}\rangle$ type system and the “prismatic edge (PrE)” in the $\langle\bar{a}\rangle$ type slip systems is in good agreement with previous TEM observations in deformed titanium [33,35].

5. Conclusions

Three type of nanostructured materials with hexagonal crystal structure were studied by X-ray diffraction profile analysis. The crystallite size distribution and the dislocation structure were determined and compared with the observations obtained by other methods.

The effect of the crystallization temperature on the grain-size distribution of silicon nitride powder was examined. It was shown that the mean size of the crystalline grains decreased slightly at temperatures up to 1450°C probably because of the crystallization of the smaller amorphous grains, while it significantly increased during heat-treatment at 1500°C. For the powder having high amount of crystalline phases

(crystallized at 1500°C) the grain-size distribution and the average grain-size obtained by X-rays were in good agreement with those determined by TEM and from the specific surface area, respectively.

The density and the character of dislocations in sintered nanocrystalline tungsten-carbide were determined. Analysing the contrast factors of dislocations it was found that the dominant slip system in this specimen is the basal edge: $\langle 1\bar{1}20 \rangle \{0001\}$. The dislocation density was found to be $1.5 \cdot 10^{16} \text{ m}^{-2}$.

The microstructure of nanostructured titanium produced by SPD was also studied. It was found that SPD produces crystallite sizes of several tens of nanometers. The dominant $\langle c+a \rangle$ type and $\langle a \rangle$ type slip systems are “pyramidal edge 4” and “prismatic edge”, respectively, which is in good agreement with previous TEM observations. Also, the crystallite size (43 nm) and dislocation density ($0.86 \cdot 10^{15} \text{ m}^{-2}$) values determined by X-rays are in good agreement with TEM results.

Acknowledgements

This work was supported by the Hungarian Scientific Research Fund, OTKA, Grant Nos. T031786, T034666 and T029701. J.G. is grateful for the financial support of Magyary Zoltán postdoctoral program of Foundation for Hungarian Higher Education and Research (AMFK).

References

1. Kuzel, Jr R.; Klimanek, P.: J. Appl. Cryst. 22 (1989) 299.
2. Ungár, T.; Borbély, A.: Appl. Phys. Lett. 69 (1996) 3173.
3. Groma, I.: Phys. Rev. B 57 (1998) 7535.
4. Wu, E.; Mac A; Gray, E; Kisi, E. H.: J. Appl. Cryst. 31 (1998) 356.
5. Scardi, P.; Leoni, M.: J. Appl. Cryst. 32 (1999) 671.
6. Cheary, R. W.; Dooryhee, E.; Lynch, P.; Armstrong, N.; Dligatch, S.; J. Appl. Cryst. 33 (2000) 1271.
7. Kamminga, J.-D.; Delhez, R.: J. Appl. Cryst. 33 (2000) 1122.
8. Solas, D. E.; Tomé, C. N.; Engler, O.; Wenk, H. R.: Acta Mater. 49 (2001) 3791.
9. Scardi, P.; Leoni, M.: Acta Cryst. A57 (2001) 604.
10. Ungár, T.; Gubicza, J.; Ribárik, G.; Borbély, A.: J. Appl. Cryst. 34 (2001) 298.
11. Ribárik, G.; Ungár, T.; Gubicza, J.: J. Appl. Cryst. 34 (2001) 669.
12. Williamson, G. K.; Hall, W. H.: Acta Metall. 1 (1953) 22.
13. Warren B. E.; Averbach, B. L.: J. Appl. Phys. 21 (1950) 595.
14. Warren B. E.: Progr. Metal Phys. 8 (1959) 147.
15. Caglioti, G.; Paoletti, A.; Ricci, F. P.: Nucl. Instrum. 3 (1958) 223.
16. Le Bail, A.: Proc. Accuracy in Powder Diffraction II, NIST Special Publication, 846 (1992) 142.
17. Krivoglaz, M. A.: *Theory of X-ray and Thermal Neutron Scattering by Real Crystals* (Plenum Press, New York 1996).
18. Wilkens, M.: phys. stat. sol. (a) 2 (1970) 359.
19. Wilkens, M.: *Fundamental Aspects of Dislocation Theory*, ed. J. A. Simmons, R. de Wit, R. Bullough, Vol. II. Nat. Bur. Stand. (US) Spec. Publ. No. 317, Washington, DC. USA, (1970) p. 1195.
20. Szépvölgyi, J.; Riley, F. L.; Mohai, I.; Bertoti, I.; Gilbart, E.: J. Mater. Chem. 6 (1996) 1175.
21. Stolyarov, V. V.; Zhu, Y. T.; Alexandrov, I. V.; Lowe, T. C.; Valiev, R. Z.: J. Nanoscience and Nanotechnology, 1 (2001) 237.
22. Wilkens, M; Eckert, H.: Z. Naturforschung, 19a (1964) 459.
23. Stokes, R: Proc. Phys. Soc. London 61 (1948) 382.
24. Dragomir, I. C.; Ungár, T.: J. Appl. Cryst., submitted.
25. Terwilliger, Ch. D.; Chiang, Y. M.: Acta Met. Mater. 43 (1995) 319.
26. Ungár, T.; Borbély, A.; Goren-Muginstein, G. R.; Berger, S.; Rosen, A. R.: Nanostructured Materials 11 (1999) 103.
27. Langford, J. I.; Louér, D.; Scardi, P.: J. Appl. Cryst. 33 (2000) 964.
28. Gubicza, J.; Szépvölgyi, J.; Mohai, I.; Ribárik, G.; Ungár, T.: J. Mat. Sci. 35 (2000) 3711.
29. Hinds, W. C.: *Aerosol Technology: Properties, Behavior and Measurement of Airbone Particles* (Wiley, New York 1982).
30. Lippenga, B. C.; Hermanns, M. A.: Powd. Met. 7 (1961) 66.
31. Gubicza, J.; Ribárik, G.; Goren-Muginstein, G. R.; Rosen A. R.; Ungár, T.: Mat. Sci. Eng. A309-310 (2001) 60.
32. Zhu, Y. T.; Huang, J.Y.; Gubicza, J.; Ungár, T.; Wang, Y.M.; Ma, E; Valiev, R. Z.: Acta Met., to be submitted.
33. Jones, I. P.; Hutchinson, W. B.: Acta Met. 29 (1981) 951.

34. Gubicza, J.; Dragomir, I. C.; Ribárik, G.; Zhu, Y. T.; Valiev, R. Z.; Ungár, T.: J. Mat. Res., submitted.
35. Kelly, A.; Groves, G. W.: Crystallography and Crystal Defects, (Longman, London 1970), pp.174

Table 1.

The amorphous phase content, the median (m) and the variance (σ) of the grain-size distribution, the area-weighted mean grain-size of the crystalline fraction and entire powder $\langle x \rangle^c_{\text{area}}$ and $\langle x \rangle^t_{\text{area}}$ in silicon nitride powders heat-treated at different temperatures.

temperature of heat-treatment	amorphous (vol%)	m [nm]	σ	$\langle x \rangle^c_{\text{area}}$ [nm]	$\langle x \rangle^t_{\text{area}}$ [nm]
as-synthesized	80	26±3	0.63±0.05	74±5	35±2
1250°C	70	23±3	0.67±0.06	72±6	51±3
1350°C	65	16±2	0.71±0.07	60±5	52±3
1450°C	25	18±2	0.67±0.06	63±6	75±3
1500°C	20	53±7	0.47±0.05	93±6	94±3

Captions

Figure 1: The measured and fitted Fourier coefficients normalized to unity for nanocrystalline titanium. The differences between the measured and fitted values are also shown in the lower part of the figure. The scaling of the differences is the same as in the main part of the figure. The indices of the reflections are also indicated.

Figure 2: The area-weighted mean grain-size of the crystalline fraction and that of the entire silicon nitride powder heat-treated at different temperatures.

Figure 3: Bar-diagram of the grain-size distribution obtained from TEM micrographs and the size distribution function, $f(x)$ (solid line), determined by X-rays for silicon nitride powder heat-treated at 1500°C.

Figure 4: The crystallite size-distribution density function, the median, the arithmetically, the area- and the volume-weighted mean crystallite sizes for tungsten-carbide specimen determined from X-ray peak profile analysis.

Fig. 1.
T. Ungár & J. Gubicza

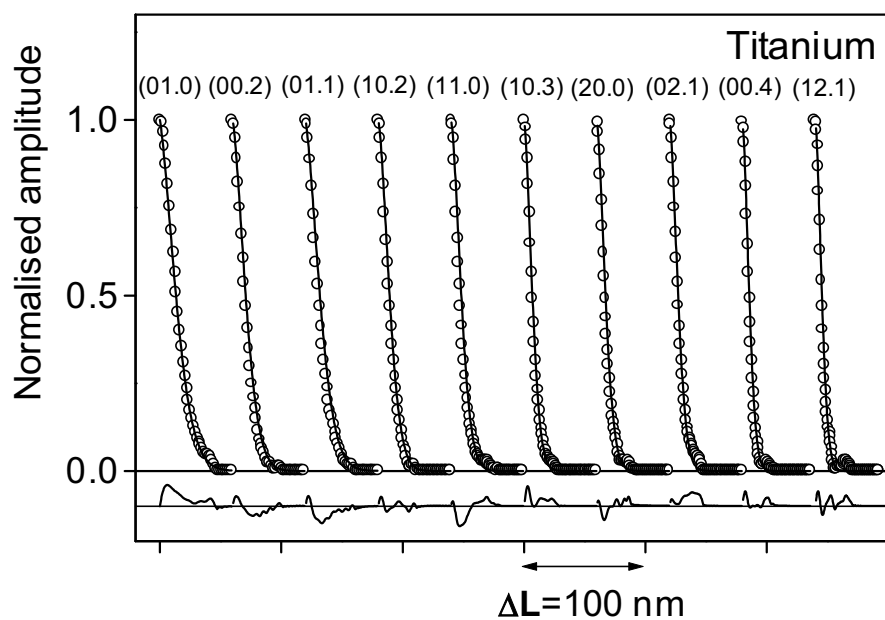


Fig. 2.
T. Ungár & J. Gubicza

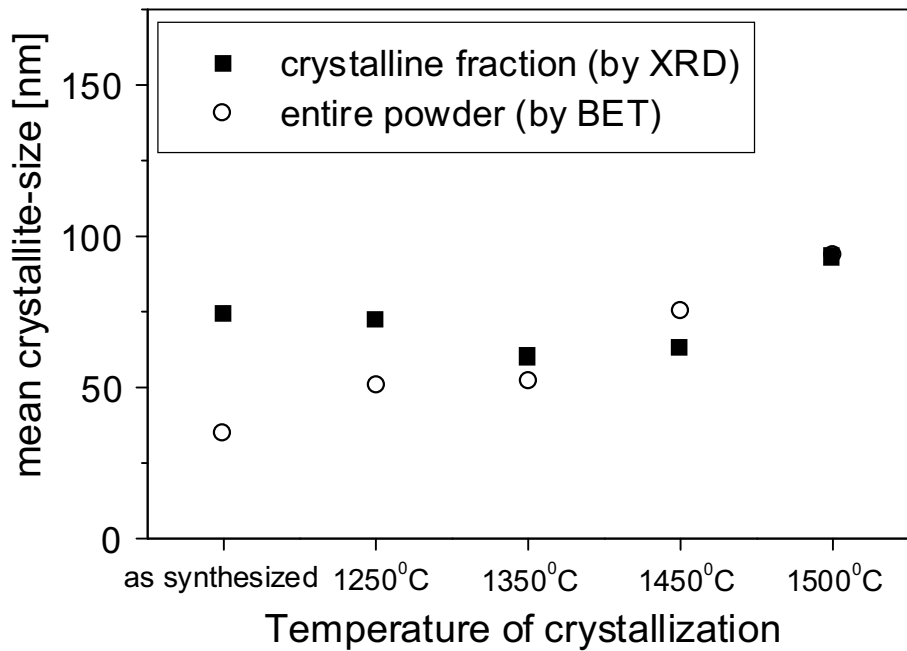


Fig. 3.
T. Ungár & J. Gubicza

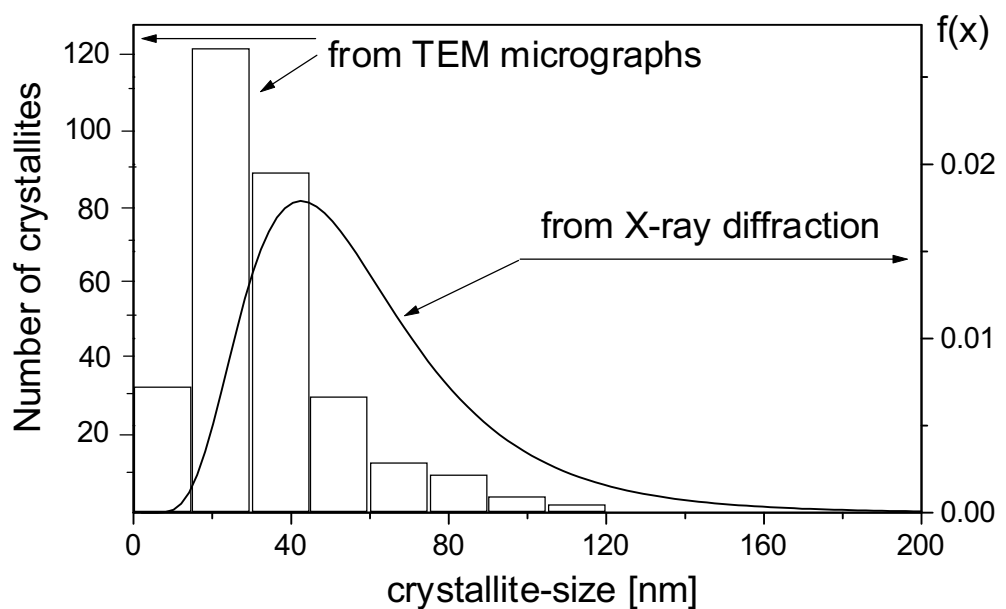


Fig. 4.
T. Ungár et al.

